(Received 21 March 2026, Accepted 10 April 2026, Scheduled 6 May 2026)

# Analysis and Optimal Design of a Novel Permanent Magnet Fault-Tolerant Vernier Rim-Driven Motor with Inclined Modulation Tooth

Defeng Zhao, Jingwei Zhu*, Yaqian Cai, and Anni Wang

*Marine Electrical Engineering College, Dalian Maritime University, Dalian 116026, China*

**ABSTRACT:** To address the trade-off between torque density and power factor in conventional permanent magnet vernier rim-driven motors under material cost constraints, this study proposes a novel permanent magnet fault-tolerant vernier rim-driven motor with an inclined modulation tooth (PMFTVRDM-IMT). Unlike the conventional straight-tooth configuration, the proposed design introduces an inclination angle to the modulation teeth, thereby altering the air-gap permeance distribution pathway while preserving both the permanent magnet volume and overall motor envelope. Through magnetic field harmonic analysis, the underlying mechanism for the synchronous improvement in the torque and power factor was revealed: the inclined modulation tooth structure enhances the effective working harmonics while suppressing the ineffective harmonic components. To further optimize the motor performance, a combined approach of single-parameter scanning and multi-objective optimization was adopted, and the resulting performance metrics, such as output torque and power factor, were systematically validated using the finite element analysis (FEA). The results indicate that, with modifications only to the modulation tooth structure, the proposed motor design achieves an approximately 15% improvement in the power factor and a 2.5% increase in the torque density, thereby substantiating the feasibility and engineering value of the inclined modulation-tooth topology in mitigating the low power factor issue inherent to vernier machines.

## 1. INTRODUCTION

Propelled by the dual forces of global energy transition and maritime decarbonization, the electrification of ship propulsion systems has emerged as a critical technological response within the industry [1]. As a key component in this technological pathway, the rim-driven motor (RDM) achieves the structural integration of a propulsion motor with the propeller. This integrated design significantly enhances the propulsion efficiency of the system and demonstrates notable advantages in reducing operational vibrations and radiated noise [2, 3].

Currently, RDMs predominantly employ induction motors or permanent magnet synchronous motors (PMSMs) [4–6].

To meet the increasing demand for torque density, the performance enhancement of conventional PMSMs has approached its limits, making the use of magnetic field modulation effects an effective approach for boosting torque. Based on this principle, a permanent magnet vernier motor (PMVM) was developed. By utilizing the harmonic modulation of the air-gap magnetic field, the PMVM significantly improves the torque density at low speeds, offering a high power density. This characteristic makes it particularly suitable for applications in which low-speed and high-torque operations are essential, including marine propeller drives [7]. Furthermore, given that rim driven thrusters (RDTs) operate underwater for extended periods and are prone to electrical faults, a fault-tolerant PMVM topology was proposed [8].

Conventional methods for improving the torque density of PMVMs focus on increasing the number and amplitude of the main working harmonics. A combined stator was proposed [9], which significantly increased the number of working harmonics, thereby enhancing the torque density of the motor while reducing the torque ripple. In [10], a coded-tooth structure was introduced, which incorporates permeance harmonics with specific amplitudes and phases to increase the torque density of the motor. In [11], the torque density was enhanced by a multi-degree-of-freedom modulator through an improved air-gap permeance. Studies [12–14] enhanced the number of working excitation flux density harmonics by introducing additional air-gap permeance harmonics, thus improving the torque density. However, these structures often reduce the power factor while increasing the torque density. To address this issue, a hybrid tooth stator vernier permanent magnet motor was proposed [15]. This configuration modifies the air-gap permeance harmonics, increases the order of the non-working armature flux density harmonics, and ultimately enhances the power factor of the motor. In [16], a vernier permanent magnet motor with a fractional-slot distributed winding spanning two teeth was proposed, which reduced the quantity of low-order, ineffective armature harmonics, leading to an improvement in the power factor. In summary, adopting suitably shaped modulator teeth can increase the proportion of working harmonics and decrease that of non-working harmonics, thereby optimizing the magnetic field modulation and effectively improving both the power factor and torque density in PMVMs [17–20].

* Corresponding author: Jingwei Zhu (zjwdl@dlmu.edu.cn).

This study proposes a novel permanent magnet fault-tolerant vernier rim-driven motor with an inclined modulation tooth (PMFTVRDM-IMT), which effectively improves the power factor and torque density by enhancing the working harmonics and suppressing the non-working harmonics. Section 2 describes the motor structure and working principles of the proposed motor. The theoretical analysis is validated through FEA, and a comparative study of the magnetic field harmonics between the PMFTVRDM-IMT and the permanent magnet fault-tolerant vernier rim-driven motor with conventional modulation-tooth (PMFTVRDM-CMT) is conducted. In Section 3, an optimization design is carried out by combining single-parameter scanning with multi-objective optimization. In Section 4, the performances of the PMFTVRDM-IMT and PMFTVRDM-CMT are compared based on the FEA results.

## 2. MOTOR STRUCTURE AND WORKING PRINCIPLE ANALYSIS

The modulation tooth alters the periodic distribution of the air-gap permeance to achieve the harmonic modulation of the magnetic field of a permanent magnet, thereby enhancing the effective working harmonics. This section systematically analyzes the permeance and magnetic flux density characteristics of the PMFTVRDM-IMT compared with those of the PMFTVRDM-CMT, elucidating the mechanisms underlying the improvements in torque and power factor.

### 2.1. Topological Structure

The structure of PMFTVRDM-IMT is shown in Fig. 1. The stator adopts an interleaved arrangement of the armature and isolation teeth. A six-phase single-layer fractional-slot concentrated winding is adopted for the stator and implemented on an inclined tooth structure. The physical separation between the phases is achieved using straight teeth, which enhances the fault tolerance capability of the motor.

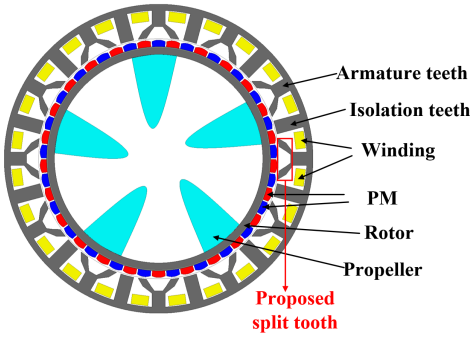


**FIGURE 1**. The structure of PMFTVRDM-IMT.

A key feature of the concentrated winding configuration is its shortened end-winding length, which leads to a lower copper loss and attenuated torque ripple. The six-phase winding consists of two symmetrical systems arranged in a $YY$ connection with a 30° electrical angle displacement. The first winding set was wound in the forward direction, whereas the second set was wound in the reverse direction. This symmetric forward-reverse winding configuration effectively cancels a significant portion of the harmonics, thereby improving the power factor and reducing the mutual inductance between the phases.

The structure of the stator modulated-tooth is shown in Fig. 2. In the PMFTVRDM-CMT, the modulation teeth are straight, with their axes perpendicular to the axial end-plane of the motor. In contrast, the proposed PMFTVRDM-IMT introduces a tangential inclination angle along the axial direction. It should be particularly noted that the radial cross-sectional profile of the modulation teeth remains rectangular. The initial structural parameters are listed in Table 1.

**TABLE 1**. Initial structural parameters.

| Items | Values |
|---|---|
| Number of Isolation Teeth | 12 |
| Number of PM Pole Pairs, $P_r$ | 25 |
| Number of Stator Slots | 24 |
| Number of Armature Teeth | 12 |
| Pole Embrace/$\alpha$ | 0.9 |
| Isolation Tooth Width | 11 mm |
| Stator Outer Diameter/$D_0$ | 255 mm |
| Rotor Outer Diameter/$D_{ro}$ | 196 mm |
| Air Gap Length/$g$ | 2 mm |
| Slot Opening Width/$b_s$ | 3.5 mm |
| Number of turns winding | 300 |

### 2.2. Analysis of Working Principle

To analyze the magnetic field modulation mechanism of motors, the following assumptions were made:

1. The magnetomotive force (MMF) of the PMs is an ideal wave.

2. The core saturation was neglected.

Based on Assumption 1, the MMF waveform of the PMs can be simplified to a square wave, as shown in Fig. 3.

Performing Fourier decomposition on it yields:

$$F_r(\theta,t) = \sum_{i=1,3,5}^{\infty} F_{ri}\cos\left[nP_r(\theta-\omega_r t)\right] \tag{1}$$

where $P_r$ is the number of rotor pole pairs; $\theta$ is the mechanical angle; $\omega_r$ is the mechanical angular velocity; and $F_{ri}$ is the amplitude of the $i$th MMF harmonic.

Owing to the combined effect of the stator slots and inclined modulation-tooth structure, the waveform of the equivalent air-gap permeance is shown in Fig. 4, where $\lambda_v$ and $\lambda_p$ are the permeabilities of air and iron core, respectively; $\theta_\alpha$ is half the dimension of the isolation tooth; $\theta_\beta$ is the dimension of the modulation tooth in the conventional motor; and $\theta_1$ and $\theta_2$ are the horizontal and inclined sections of the modulation tooth in the proposed motor, respectively; $\theta_3$ and $\theta_r$ are half of the upper width of the slot opening in the proposed and conventional motors, respectively; $\theta_s$ is the angle between the centerline of the modulation tooth and a predefined mechanical reference position of the motor.

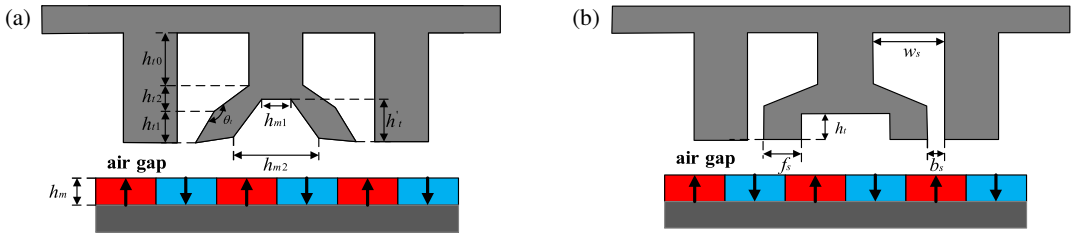


**FIGURE 2**. Stator tooth structure of two motors. (a) The PMFTVRDM-IMT; (b) The PMFTVRDM-CMT.

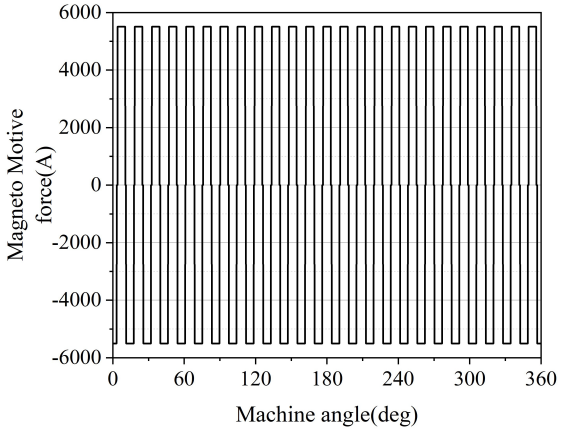


**FIGURE 3**. Waveform of the MMF of PMs.

The expression for the air-gap permeance is as follows:

$$\begin{cases} \lambda_s(\theta) = \lambda_{s0} + \sum_{i=1}^{\infty} \lambda_{si} \cos\left[iZ(\theta - \theta_s)\right] \\ \lambda'_s(\theta) = \lambda'_{s0} + \sum_{i=1}^{\infty} \lambda'_{si} \cos\left[iZ(\theta - \theta_s)\right] \end{cases} \quad (2)$$

where $\lambda_{s0}$ and $\lambda_{si}$ are the DC component and amplitude of the $i$th harmonic of the air-gap permeance in the conventional motor; $\lambda'_{s0}$ and $\lambda'_{si}$ are the DC component and amplitude of the $i$th harmonic of the air-gap permeance in the proposed motor, respectively; and $Z$ is the number of armature teeth.

Under the premise of considering only the DC component of the MMF, based on Equations (1) and (2), the air-gap magnetic flux density owing to the PMs is given by

$$B_r(\theta,t) = B_{rpm0}\cos\left[P_r(\theta - \omega_r t)\right] + \sum_{i=1}^{\infty} B_{rpmi}\cos\left[(P_r + iZ)\theta - (P_r\omega_r t + iZ\theta_s)\right] + \sum_{i=1}^{\infty} B_{rpmi}\cos\left[(P_r - iZ)\theta - (P_r\omega_r t - iZ\theta_s)\right] \quad (3)$$

where $B_{rpm0}$ is the fundamental magnetic flux field, and $B_{rpmi}$ is the harmonic component of the modulated magnetic flux field.

For the PMFTVRDM-IMT:

$$B_{rpm0} = F_{r1}\left[\lambda_V + \frac{Z(\theta_\alpha + \theta_1 + \theta_2/2)}{\pi}(\lambda_p - \lambda_v)\right]$$

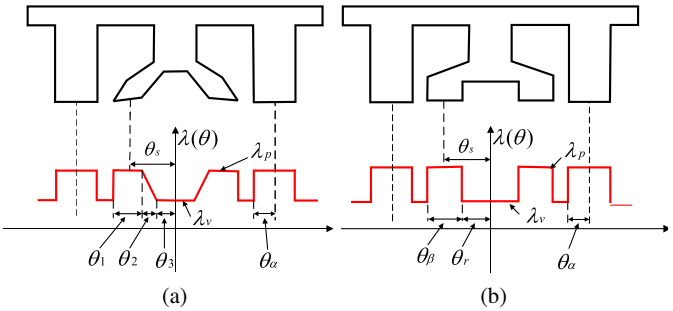


**FIGURE 4**. Equivalent magnetic permeability: (a) The PMFTVRDM-IMT; (b) The PMFTVRDM-CMT.

$$B_{rpmi} = \frac{F_{r1}(\lambda_p - \lambda_v)}{i\pi}\left[\begin{array}{l}\sin(iZ(\theta_1+\theta_2+\theta_3))+ \\ \frac{\cos(iZ(\theta_2+\theta_3))-\cos(iZ\theta_3)}{iZ\theta_2} \\ +(-1)^i\sin(iZ\alpha)\end{array}\right] \quad (4)$$

For the PMFTVRDM-CMT:

$$B_{rpm0} = F_{r1}\left[\lambda_v + \frac{Z(\theta_\alpha + \theta_\beta)}{\pi}(\lambda_p - \lambda_v)\right]$$

$$B_{rpmi} = \frac{F_{r1}(\lambda_p - \lambda_v)}{i\pi}\left[\sin(iZ(\theta_\gamma + \theta_\beta)) - \sin(iZ\theta_\gamma) - (-1)^i\sin(iZ\theta_\alpha)\right] \quad (5)$$

According to (3), the orders and rotational speeds of the dominant working harmonics generated by the PM MMF are listed in Table 2.

**TABLE 2**. Harmonic of magnetic flux density operation of PMs.

| Items | Order | Speed | Examples | |
|---|---|---|---|---|
| | | | order | speed |
| PMs | $P_r$ | $\omega_r$ | 25th | 1 |
| | $P_r + iz$ | $\frac{P_r\omega_r}{P_r+iz}$ | 37th, 49th... | 25/37, 25/49... |
| | $\lvert P_r - iz\rvert$ | $\frac{P_r\omega_r}{\lvert P_r-iz\rvert}$ | 1th, 11th... | 1/25, 11/25, 13/25... |

The analytical and FEA results for the air-gap flux density are plotted in Fig. 5. Minor discrepancies exist near the magnetic edges, waveform troughs, and peaks, which are attributable to the interpolar leakage flux.

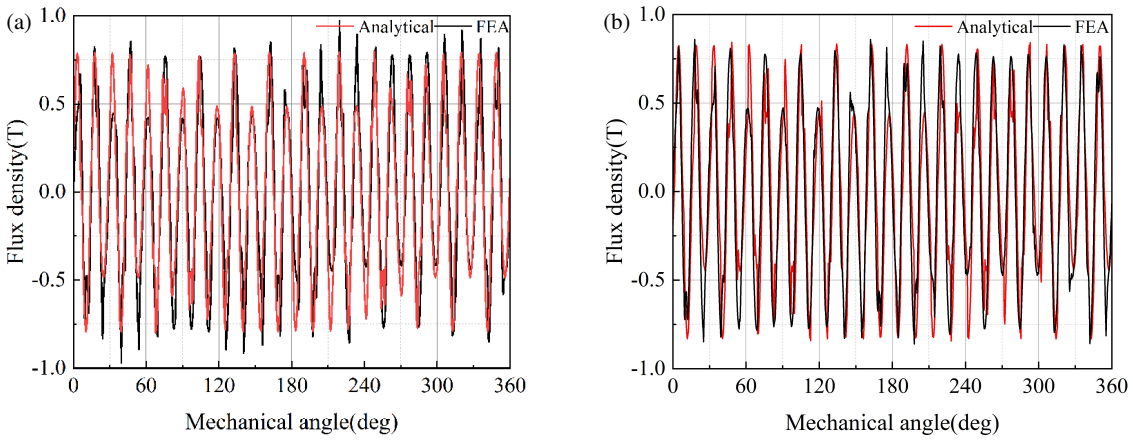


**FIGURE 5**. Comparative results of the two methods: (a) The PMFTVRDM-IMT; (b) The PMFTVRDM-CMT.

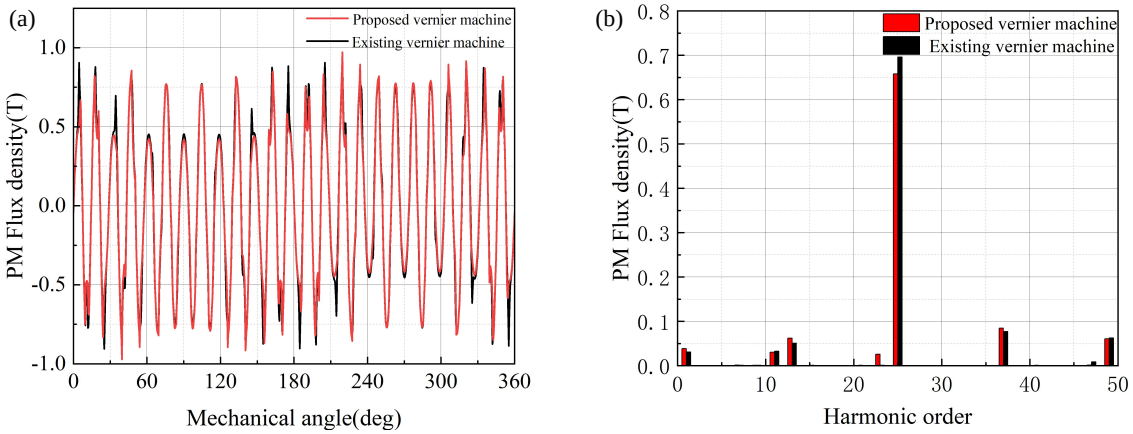


**FIGURE 6**. Comparison of flux density of the PMs: (a) Waveforms; (b) Spectrums.

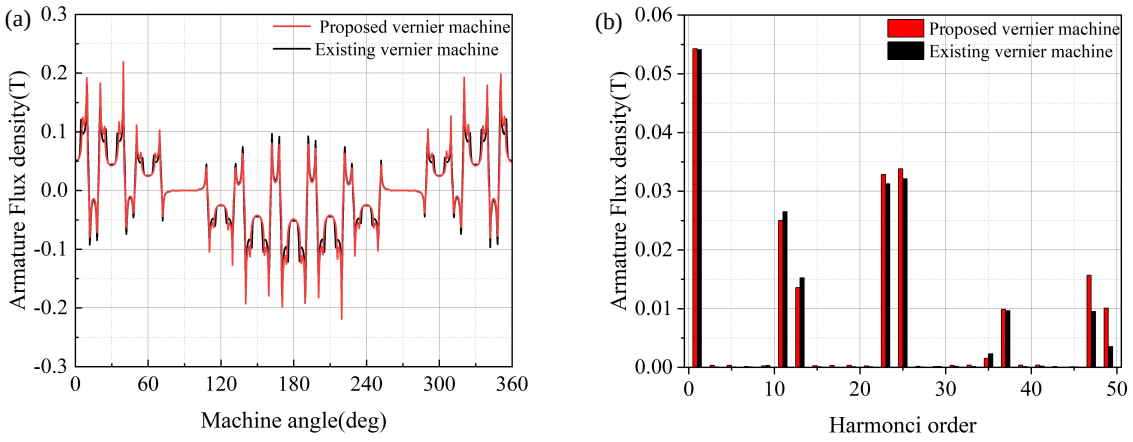


**FIGURE 7**. Comparison of flux density of armature winding: (a) Waveforms; (b) Spectrums.

### 2.3. Mechanism of Performance Enhancement

Both motors are magnetic-field-modulated motors, in which the magnetic field generated by the PMs interacts with the armature magnetic field after modulation, thereby enhancing torque density. This subsection provides an analysis of the torque and power factor improvement mechanisms from the magnetic field perspective.

FEA was performed on the PMs and armature magnetic fields of both PMFTVRDM-IMT and PMFTVRDM-CMT. The results are shown in Figs. 6 and 7. The analysis revealed that the PM magnetic field distributions of the two motors were relatively similar. The primary reason for this is that the magnetic reluctance encountered by the flux generated by the PMs across the air-gap circumference is less affected by variations

in the modulation tooth structure, resulting in essentially consistent magnetic flux paths in both designs. However, an analysis of the armature magnetic field, with higher-order harmonics neglected, reveals that in the proposed motor, the working harmonic amplitude is boosted by 19.19%, whereas the non-working harmonic amplitude is cut by 48.81% relative to the conventional motor. This marked optimization in the harmonic composition, which reduces the proportion of non-working harmonics, directly contributes to the overall performance gains in torque and power factor.

## 3. ANALYSIS AND OPTIMIZATION OF STRUCTURAL PARAMETERS

This section analyzes and optimizes the PMFTVRDM-IMT to maximize the average torque and power factor. Five structural parameters were used as optimization variables: the rotor PMs thickness $h_m$, upper width $h_{m1}$ and lower width $h_{m2}$ of the auxiliary slot, slot opening height $h_t$, and tilt angle $\theta_t$ of the inclined modulation tooth.

### 3.1. Parameter Analysis

The influence of $h_m$ on the optimization objectives is shown in Fig. 8. The maximum average torque was achieved at a thickness of 5.5 mm. Although the power factor continued to increase with increasing magnet thickness, the extent of improvement was marginal. Furthermore, increasing the magnet thickness reduces the torque and increases the cost. Considering these factors, the thickness of the permanent magnet was set to 5.5 mm.

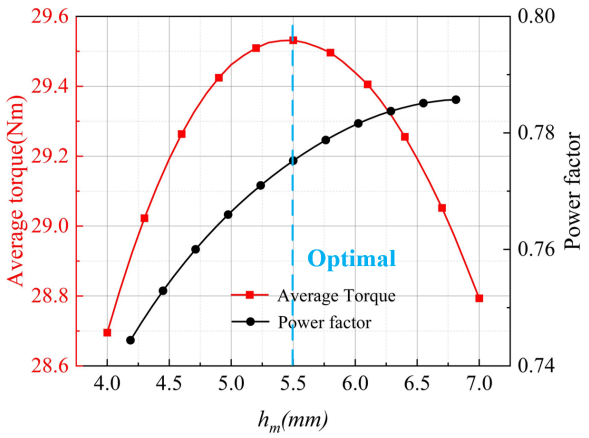


**FIGURE 8**. Influence of $h_m$ on the optimization objective.

Figures 9(a) and (b) show the influence of $\theta_t$ and $h_t$ on the optimization objectives, respectively. As shown in the figures, as $\theta_t$ increases, the average torque rises to a peak and then falls, whereas the power factor initially increases slightly before dropping sharply. The variation trends of the average torque and power factor with $h_t$ are essentially similar to those with $\theta_t$. When $\theta_t = 152.8°$ and $h_t = 10.3$ mm, the maximum average torque and power factor can be achieved simultaneously.

Figures 10(a) and (b) show the effects of $h_{m1}$ and $h_{m2}$ on the average torque and power factor, respectively. As $h_{m1}$ and $h_{m2}$ increase, the average torque initially increases but subsequently decreases, whereas the power factor shows a continuous increasing trend. Because it is difficult to simultaneously achieve both the maximum average torque and maximum power factor by adjusting $h_{m1}$ and $h_{m2}$, these two parameters will be the focus of subsequent multi-objective optimization.

### 3.2. Multi-Objective Optimization

Based on the preceding analysis, parameters $h_m$, $h_t$, and $\theta_t$ can be optimized simultaneously. Subsequently, a multi-objective optimization of the proposed motor's $h_{m1}$ and $h_{m2}$ was carried out. The objectives and structure of the multi-objective optimization model can be expressed as:

Objective Functions:

$$\{\max[T_{avg}(x_i), \max[Pf(x_i)]\} \tag{6}$$

Variables and Ranges:

$$x_i = [h_{m1}, h_{m2}] \tag{7}$$

$$\begin{cases} 7\,\text{mm} \le h_{m1} \le 10\,\text{mm} \\ 17\,\text{mm} \le h_{m2} \le 25\,\text{mm} \end{cases} \tag{8}$$

where $x_i$ is the optimization variable; $T_{avg}(x_i)$ and $Pf(x_i)$ are the average torque and power factor corresponding to each variable, respectively.

The optimization employs a Multi-Objective Genetic Algorithm (MOGA), yielding a set of feasible solutions, as graphically summarized in Fig. 11. A trade-off exists between achieving the maximum average torque and power factor, which requires a compromise. Based on this, the red point was chosen as the optimal design, and the optimized motor parameters are listed in Table 3.

**TABLE 3**. The motor parameters before and after optimization.

| Items | Before optimization | After optimization |
|---|---|---|
| $\theta_t(°)$ | 160 | 152.8 |
| $h_t$ (mm) | 8.4 | 9.3 |
| $h_{m1}$ (mm) | 6 | 8.4 |
| $h_{m2}$ (mm) | 17.9 | 18.7 |
| $h_m$ (mm) | 5.8 | 5.5 |

## 4. PERFORMANCE COMPARISON

To ensure a fair comparison, both motors underwent identical optimization processes prior to performance evaluation.

### 4.1. No-Load Back EMF

Figure 12 compares the no-load back EMF waveforms. The analysis results indicate that while the total harmonic distortion (THD) of both the PMFTVRDM-IMT and PMFTVRDM-CMT is 1.95%, the proposed motor exhibits a larger back-EMF amplitude than the conventional one.

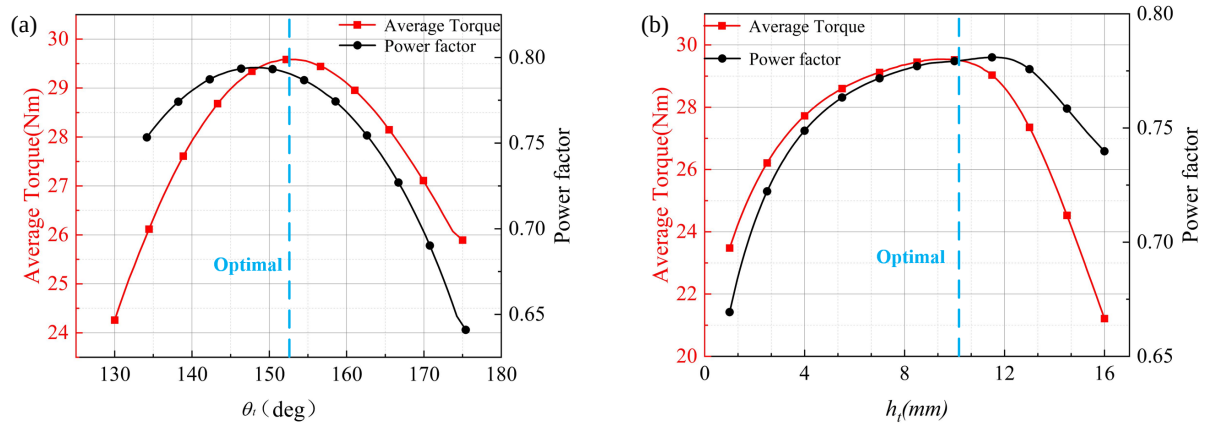


**FIGURE 9**. Influence of parameters on the optimization objective: (a) $\theta_t$; (b) $h_t$.

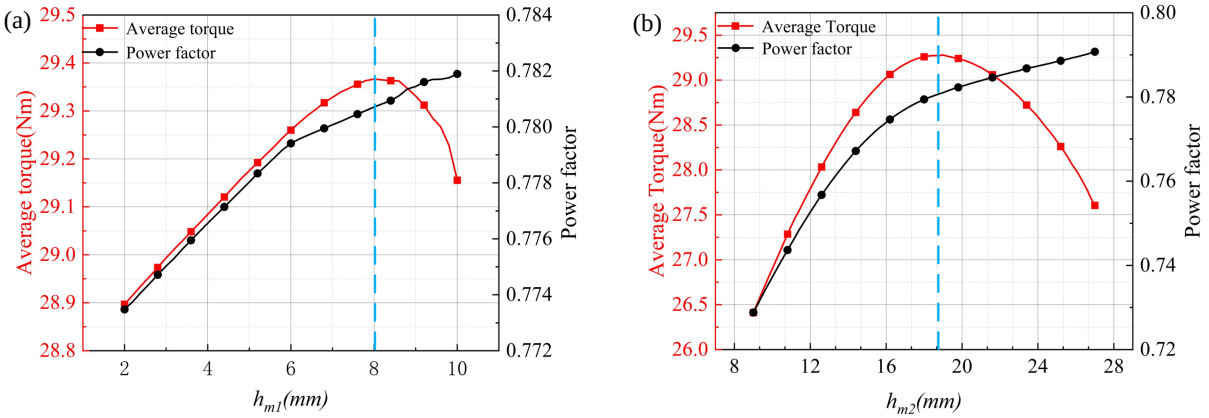


**FIGURE 10**. Influence of parameters on the optimization objective: (a) $h_{m1}$; (b) $h_{m2}$.

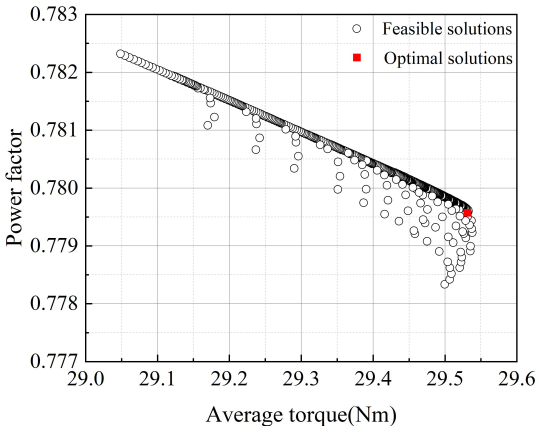


**FIGURE 11**. Feasible solution points for optimization.

### 4.2. Torque and Power Factor

Figure 13 compares the variation in torque and power factor with current for the two motor designs. Under rated operating conditions, the PMFTVRDM-IMT exhibited a 15% improvement in the power factor and a 2.5% increase in torque compared with the PMFTVRDM-CMT.

### 4.3. Inductance & Fault Tolerance

Taking phase A as an example, Fig. 14 presents a comparison of the self-inductance and mutual inductance for both motors, with their respective maximum self-inductance values reaching 22.13 mH and 28.4 mH. A reduction in inductance can improve the power factor of the motors. Their respective maximum mutual inductance values were 0.148 mH and 0.16 mH. Based on these values, the coupling coefficients were calculated as 0.67% and 0.56%, respectively.

The PMFTVRDM-IMT possesses a marginally higher coupling coefficient than the PMFTVRDM-CMT, due to the reduction in its self-inductance. The mutual inductance of the PMFTVRDM-IMT was lower than that of the PMFTVRDM-CMT. A reduction in the mutual inductance can enhance the magnetic isolation capability of the motor. Therefore, the PMFTVRDM-IMT still possesses a strong fault-tolerance capability.

### 4.4. Torque Ripple

Figure 15 compares the torque ripple. The torque ripple coefficient of the PMFTVRDM-IMT is 0.0268%, while that of the PMFTVRDM-CMT is 0.0406%, representing a reduction of approximately 34%. The peak-to-peak torque ripple of the PMFTVRDM-IMT is 0.115%, whereas that of the

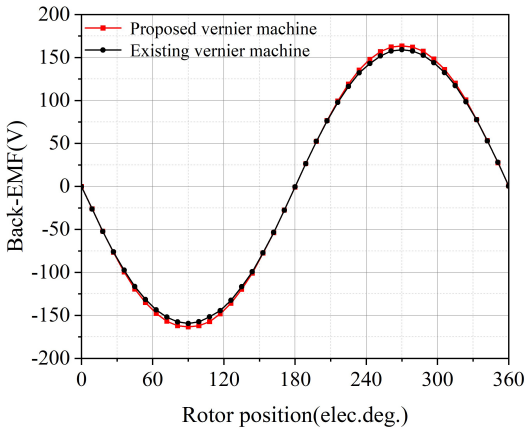


**FIGURE 12**. Comparison of no-load counter electromotive force.

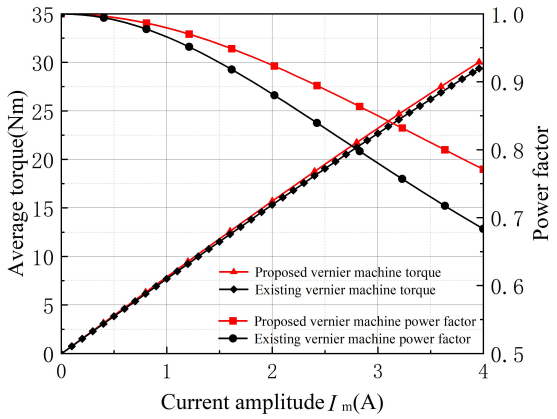


**FIGURE 13**. Comparison of torque and power factor.

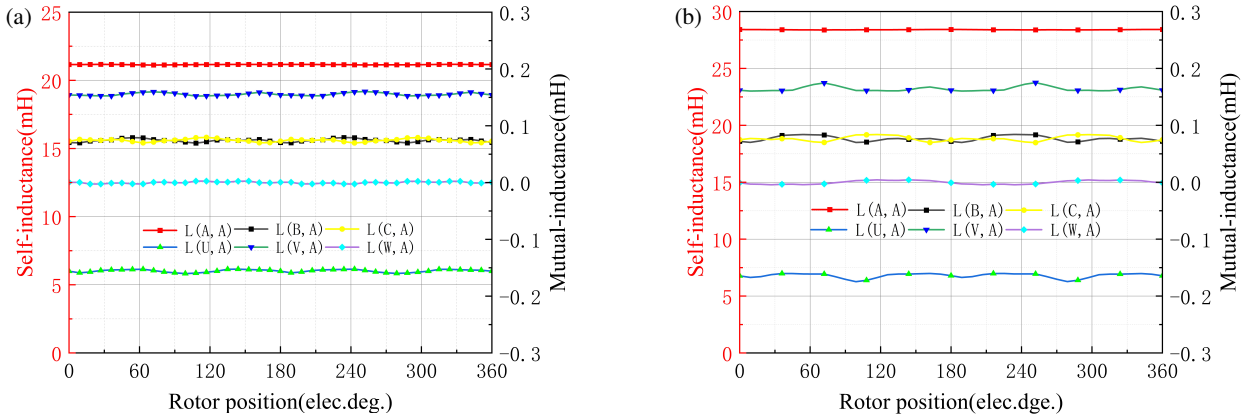


**FIGURE 14**. Self-inductance and mutual inductance: (a) The PMFTVRDM-IMT; (b) The PMFTVRDM-CMT.

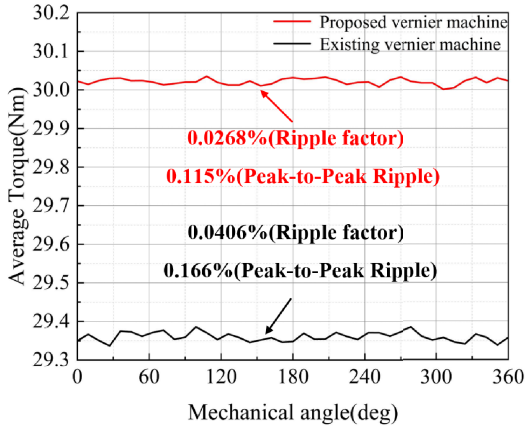


**FIGURE 15**. Comparison of torque ripple.

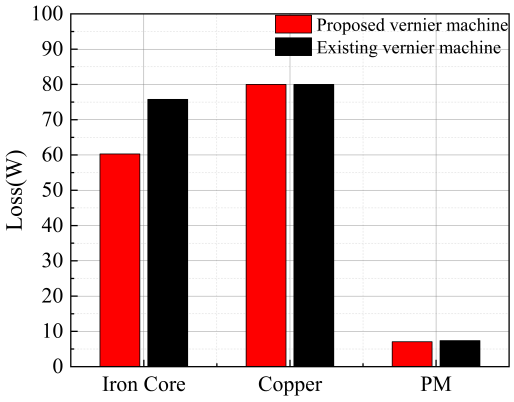


**FIGURE 16**. Comparison of losses.

PMFTVRDM-CMT is 0.166%, corresponding to a decrease of about 30.7%. Both metrics indicate that the torque smoothness of the PMFTVRDM-IMT is significantly superior to that of the PMFTVRDM-CMT.

### 4.5. Loss

Figure 16 compares the losses of the two machines at an electrical loading of 160 A/cm. It can be concluded that the copper losses of the two machines are identical, because both employ the same number of winding turns, identical wire diameter, and the same current. Furthermore, the permanent magnet loss of the PMFTVRDM-IMT is slightly decreased by about 4.1%. The iron loss of the PMFTVRDM-IMT is reduced by approximately 20.4%. This reduction is primarily attributed to the substantial suppression of non-working harmonics in the armature magnetic field, which alleviates high-frequency alternating magnetization within the iron core.

## 5. CONCLUSION

This study proposes an inclined modulation-tooth structure capable of improving the torque density and power factor. Theoretical analysis reveals that the power factor enhancement benefits from the effective suppression of non-working harmonics by the proposed structure, whereas the increased torque density is primarily attributed to the significant augmentation of the working harmonic content. Employing a single-parameter scanning method reduced the number of optimization variables and determined their optimal ranges, enabling the comprehensive optimization of both motors with a relatively low computational effort. Finally, the FEA results indicated that, compared with the PMFTVRDM-CMT, the PMFTVRDM-IMT achieved an approximately 15% improvement in power factor and a 2.5% increase in torque density. Future work will focus on prototype fabrication and experimental validation, along with further investigation into the thermal and mechanical behavior of the inclined modulation-tooth under practical operating conditions.

## ACKNOWLEDGEMENT

This work was supported in part by the National Natural Science Foundation of China under Grant 52377037.

## REFERENCES

[1] Zang, K., J. Zhu, H. Liao, and Y. Cai, "Performance comparison of fault-tolerant permanent magnet vernier rim-driven machines with different winding distributions," *Journal of Power Electronics*, Vol. 26, No. 3, 684–695, 2026.

[2] Liang, Z., X. Ren, D. Li, R. Qu, and X. Han, "Analysis of a spoke-array brushless dual-electrical-port dual-mechanical-port machine with reluctance rotor," *IEEE Transactions on Industrial Electronics*, Vol. 68, No. 4, 2999–3011, 2021.

[3] Yanamoto, T., M. Izumi, M. Yokoyama, and K. Umemoto, "Electric propulsion motor development for commercial ships in japan," *Proceedings of the IEEE*, Vol. 103, No. 12, 2333–2343, 2015.

[4] Zhao, H., H. H. Eldeeb, Y. Zhan, Z. Ren, G. Xu, and O. A. Mohammed, "Robust electromagnetic design of double-canned IM for submergible rim driven thrusters to reduce losses and vibration," *IEEE Transactions on Energy Conversion*, Vol. 35, No. 4, 2045–2055, 2020.

[5] Ojaghlu, P. and A. Vahedi, "Specification and design of ring winding axial flux motor for rim-driven thruster of ship electric propulsion," *IEEE Transactions on Vehicular Technology*, Vol. 68, No. 2, 1318–1326, 2019.

[6] Cheng, B., G. Pan, and Y. Cao, "Analytical design of the integrated motor used in a hubless rim-driven propulsor," *IET Electric Power Applications*, Vol. 13, No. 9, 1255–1262, 2019.

[7] Cai, Y., J. Zhu, K. Zang, and H. Liao, "Design and performance analysis of a novel flux-concentrating fault tolerant permanent magnet vernier machine for rim driven thruster," *Journal of Power Electronics*, Vol. 25, No. 5, 849–858, 2025.

[8] Wang, Z., J. Zhu, W. He, J. Yue, and T. Zhao, "Analysis and optimization of fault tolerant permanent magnet vernier rim driven machine based on the continuous variable magnetic network model," *Journal of Electrical Engineering & Technology*, Vol. 19, No. 5, 3233–3246, 2024.

[9] Qiao, T., J. Zhu, and X. Wang, "Design and optimization of a flux-modulated fault-tolerant permanent magnet rim-driven machine with combined stator to improve torque density," *IEEE Transactions on Energy Conversion*, Vol. 38, No. 1, 75–88, 2023.

[10] Fang, L., D. Li, X. Ren, and R. Qu, "A novel permanent magnet vernier machine with coding-shaped tooth," *IEEE Transactions on Industrial Electronics*, Vol. 69, No. 6, 6058–6068, 2022.

[11] Wang, R., B. Wang, D. Tian, H. Cai, M. Cheng, and W. Hua, "Slot-pole combination analysis of FSCW-PMVM on magnetic field modulation performance," *IEEE Transactions on Transportation Electrification*, Vol. 11, No. 2, 5665–5675, 2025.

[12] Zou, T., D. Li, R. Qu, D. Jiang, and J. Li, "Advanced high torque density PM vernier machine with multiple working harmonics," *IEEE Transactions on Industry Applications*, Vol. 53, No. 6, 5295–5304, 2017.

[13] Liu, W. and T. A. Lipo, "Analysis of consequent pole spoke type vernier permanent magnet machine with alternating flux barrier design," *IEEE Transactions on Industry Applications*, Vol. 54, No. 6, 5918–5929, 2018.

[14] Gao, Y., R. Qu, D. Li, J. Li, and G. Zhou, "Consequent-pole flux-reversal permanent-magnet machine for electric vehicle propulsion," *IEEE Transactions on Applied Superconductivity*, Vol. 26, No. 4, 1–5, 2016.

[15] Du, K., L. Xu, W. Zhao, and G. Liu, "Analysis and design of a fault-tolerant permanent magnet vernier machine with improved power factor," *IEEE Transactions on Industrial Electronics*, Vol. 69, No. 5, 4353–4363, 2022.

[16] Liu, Y., H. Y. Li, and Z. Q. Zhu, "A high-power factor vernier machine with coil pitch of two slot pitches," *IEEE Transactions on Magnetics*, Vol. 54, No. 11, 1–5, 2018.

[17] Zhao, Y., D. Li, Z. Liang, and R. Qu, "A high power factor PM vernier machine with segmented stator," *IEEE Transactions on Transportation Electrification*, Vol. 10, No. 4, 9294–9303, 2024.

[18] Zhao, Y., X. Ren, X. Fan, D. Li, and R. Qu, "A high power factor permanent magnet vernier machine with modular stator and yokeless rotor," *IEEE Transactions on Industrial Electronics*, Vol. 70, No. 7, 7141–7152, 2023.

[19] Zhao, Y., D. Li, X. Ren, Z. Liang, and R. Qu, "Low pole-pair ratio integration design of permanent magnet vernier machine with improved power factor," *IEEE Transactions on Industrial Electronics*, Vol. 71, No. 3, 2820–2830, 2024.

[20] Citroni, R., F. Mangini, and F. Frezza, "Efficient integration of ultra-low power techniques and energy harvesting in self-sufficient devices: A comprehensive overview of current progress and future directions," *Sensors*, Vol. 24, No. 14, 4471, 2024.